PHYSICAL REVIEW B **95**, 035307 (2017)

# Anomalous Fraunhofer interference in epitaxial superconductor-semiconductor Josephson junctions

H. J. Suominen,[1] J. Danon,[1,2] M. Kjaergaard,[1] K. Flensberg,[1] J. Shabani,[3,*] C. J. Palmstrøm,[3,4,5]
F. Nichele,[1] and C. M. Marcus[1,†]
[1]*Center for Quantum Devices and Station Q Copenhagen, Niels Bohr Institute, University of Copenhagen, Universitetsparken 5, 2100 Copenhagen, Denmark*
[2]*Department of Physics, Norwegian University of Science and Technology, NO-7491 Trondheim, Norway*
[3]*California NanoSystems Institute, University of California, Santa Barbara, California 93106, USA*
[4]*Department of Electrical Engineering, University of California, Santa Barbara, California 93106, USA*
[5]*Materials Department, University of California, Santa Barbara, California 93106, USA*

(Received 1 November 2016; published 18 January 2017)

We investigate patterns of critical current as a function of perpendicular and in-plane magnetic fields in superconductor-semiconductor-superconductor (SNS) junctions based on InAs/InGaAs heterostructures with an epitaxial Al layer. This material system is of interest due to its exceptionally good superconductor-semiconductor coupling, as well as large spin-orbit interaction and $g$ factor in the semiconductor. Thin epitaxial Al allows the application of large in-plane field without destroying superconductivity. For fields perpendicular to the junction, flux focusing results in aperiodic node spacings in the pattern of critical currents known as Fraunhofer patterns by analogy to the related interference effect in optics. Adding an in-plane field yields two further anomalies in the pattern. First, higher-order nodes are systematically strengthened, indicating current flow along the edges of the device, as a result of confinement of Andreev states driven by an induced flux dipole; second, asymmetries in the interference appear that depend on the field direction and magnitude. A model is presented, showing good agreement with experiment, elucidating the roles of flux focusing, Zeeman and spin-orbit coupling, and disorder in producing these effects.

DOI: 10.1103/PhysRevB.95.035307

## I. INTRODUCTION

Materials with strong spin-orbit interaction (SOI) and large Zeeman splitting coupled to superconductors have attracted a great deal of attention in recent years, largely due to the possibility of accessing topological states of matter [1,2]. Despite considerable progress on such systems using semiconducting nanowires [3–6], work on two-dimensional platforms, more amenable for quantum computation schemes [7], has been limited.

The strong SOI and large Landé $g$ factor in InAs [8–10] in combination with its natural surface accumulation layer, facilitating coupling to superconductors, make the InAs two-dimensional electron gas (2DEG) a favorable candidate for creating superconductor-semiconductor hybrids [11–13]. Very recently, two-dimensional epitaxial Al/InAs heterostructures have been realized, demonstrating an exceptionally transparent superconductor-semiconductor interface, resulting in a near unity Andreev reflection probability [14–16].

Despite showing great promise, many properties of these two-dimensional epitaxial structures are not yet well understood. For instance, basic quantities such as the strength of the SOI in the hybrid system or the orientation of the resulting effective spin-orbit field are not known. Also, the detailed interplay of superconductivity, SOI, and Zeeman interaction has, to large extent, not been experimentally investigated in two-dimensional systems. Recent investigations of this interplay in the two-dimensional topological insulator HgTe have shown promising results stimulating further studies in more conventional material systems [17]. Further, since most envisioned applications of these systems require considerable in-plane magnetic fields, it is important to understand the detailed behavior of the heterostructure under applied magnetic fields with different orientations.

Superconductor-normal-superconductor (SNS) junctions form a well-established platform to study the properties of superconducting hybrid structures. SNS junctions based on semiconductors with strong SOI have been proposed to study the topological phase transition [18–21], but could also potentially be used to quantify the strength of SOI in the semiconductor [22]. For instance, theoretical models have been developed to understand how the detailed SNS current-phase relation depends on SOI in two-dimensional junctions [23], as well as in single-channel junctions [24], quantum point contacts [25,26], and nanowires [27].

Many details of the physics occurring in the junction are also encoded in the critical current. A measurement of the critical current as a function of the out-of-plane magnetic field $B_z$ is paradigmatic in the study of SNS junctions. For increasing $B_z$, the winding of the superconducting phase by the enclosed flux leads to a characteristic modulation of the critical current $I_c$. For a rectangular junction with uniform current density,

$$I_c(B_z) = I_c^{(0)} \left| \frac{\sin(\pi B_z L W/\Phi_0)}{(\pi B_z L W/\Phi_0)} \right|, \tag{1}$$

reminiscent of a single-slit Fraunhofer interference pattern in optics [28]. Here, $L$ and $W$ are the length and width of the normal region, respectively, $I_c^{(0)}$ is the zero-field critical

---

[*] Now at City College, City University of New York.

[†] marcus@nbi.ku.dk

current, and $\Phi_0 = h/2e$ is the flux quantum. This behavior has been observed in a wide variety of systems [29,30] including 2DEGs with strong SOI [31]. Deviations from this Fraunhofer form can yield information about the local magnetic field profile [32] as well as the supercurrent density in the junction [33,34]. Recently, such interference mapping has been used to probe edge states arising in two-dimensional topological insulators [35–37] and graphene [38].

In this paper, we present an experimental and theoretical study of the magnetic field dependence of the interference pattern of critical currents in epitaxial Al/InAs/Al junctions, with both perpendicular field as well as a separately controlled in-plane field. We identify several interesting effects: (i) in a purely perpendicular field, we observe a deviation from a simple Fraunhofer pattern [Eq. (1)], which we interpret as arising from flux focusing due to the Meissner effect in the epitaxial Al leads. (ii) The interference pattern changes dramatically when an in-plane field is applied. A crossover is observed in the perpendicular-field interference pattern with increasing in-plane field, from a Fraunhofer-like pattern with rapidly decreasing critical currents with node index, toward one resembling that of a superconducting quantum interference device (SQUID) with critical currents that depend only weakly on node index. We interpret this transition as again resulting from flux focusing: When the *in-plane* flux is excluded from the leads, an effective *out-of-plane* flux dipole appears in the junction region. This dipole dephases contributions to the supercurrent in the center of the junction, resulting in coherent transport only near the edges of the sample. (iii) Application of an in-plane field also induces striking asymmetries (upon reversing perpendicular field) in the interference pattern that depend on the magnitude and direction of the in-plane field, but also vary strongly from lobe to lobe and from sample to sample. Based on these observations, we conclude that flux focusing plays a key role in planar epitaxial devices, particularly in the presence of an in-plane field. Indeed, field modulations due to flux focusing may prove useful, for instance providing magnetic confinement of Andreev states. In the present devices, observation (iii)—asymmetries in the interference pattern—is dominated by disorder effects, masking related effects due to spin-orbit and Zeeman coupling.

The paper is organized as follows. Section II provides details on device fabrication and magnetotransport measurements. Section III describes the behavior of the junction with a purely perpendicular magnetic field. Section IV describes junction behavior when the applied field is purely in-plane. Section V reports effects of combined perpendicular and in-plane fields. Conclusions and open questions are discussed in Sec. VI.

## II. METHODS

The wafer structure, starting at the top surface, consists of 10 nm Al, 7 nm InAs, 4 nm $\mathrm{In_{0.81}Ga_{0.19}As}$, grown on an InAlAs buffer on an InP substrate by molecular beam epitaxy (see Ref. [39] for more details). The *in situ* epitaxial growth of the Al layer contrasts with previous approaches to 2D semiconductor-superconductor systems, where the superconductor was deposited in a subsequent processing step [36,37,40,41]. The clean interface provides high transparency [14,16] and a hard induced gap in the semiconductor [15].

Devices are patterned with conventional electron-beam lithography. In the first processing step, mesas are defined using a wet etch (220:3:3 $\mathrm{H_2O : H_3PO_4 : H_2O_2}$), followed by selective etching of Al using Transene type-D to form the junction. Atomic layer deposition is then used to form an $\mathrm{Al_2O_3}$ (40 nm) dielectric, followed by electron-beam deposition of a Ti/Au (5/250 nm) metallic top gate. Ohmic contact is provided directly by the epitaxial Al, which is electrically contacted by wire bonding.

Measurements were carried out in a dilution refrigerator at base temperature ~30 mK applying a dc+ac current bias and measuring a four-terminal voltage $V$ with standard lock-in techniques (below 100 Hz), using an ac excitation of 4 nA or less.

Characterization of the epitaxial Al film yielded a superconducting transition temperature of $T_c = 1.5$ K, and collapse of superconductivity at an out-of-plane critical field $B_{z,c} \sim 30$ mT, and an in-plane critical field $B_{r,c} \sim 1.6$ T (see Ref. [39]). Separate transport measurements of the InAs quantum well (QW) with Al removed demonstrated an electron density of $n_e = 3.8 \times 10^{16}\ \mathrm{m^{-2}}$ and mobility $\mu = 0.43\ \mathrm{m^2\,V^{-1}\,s^{-1}}$ at zero gate voltage, yielding a mean free path $l_e = 140$ nm. In this density regime, two QW subbands are occupied, as determined by magnetotransport measurements. Upon partially depleting the 2DEG with the top gate, the single subband limit is reached at gate voltage $V_\mathrm{g} < -2.0$ V with a mobility peak $\mu = 0.7\ \mathrm{m^2\,V^{-1}\,s^{-1}}$ for $n_e = 1.9 \times 10^{16}\ \mathrm{m^{-2}}$. The data presented in Secs. III to V were all obtained with $V_g = 0$. Occupation of the second subband appears to play only a minor role in all device characteristics (see Appendix B). Measurements on similar QWs have demonstrated large SOI, characterized by a spin-orbit length $l_\mathrm{so} \sim 45$ nm [14]. The superconducting coherence length is estimated as $\xi = \hbar v_\mathrm{F}/\Delta^* = 1.3\ \mu\mathrm{m}$,[1] with $v_\mathrm{F}$ the Fermi velocity and the induced superconducting gap $\Delta^* \sim 180\ \mu\mathrm{eV}$ as determined from tunneling measurements (see Ref. [15] and Supplemental Material therein).

Measurements were performed on six SNS devices, all of which showed qualitatively similar behavior (see Ref. [39]). The data in Sec. III through Sec. V A were characteristic of all devices. Data similar to those presented in Sec. V B were obtained from several samples but with broad quantitative variation, as discussed below. We focus on data from one SNS junction with contact separation, $L = 450$ nm, and lateral width, $W = 1.5\ \mu$m in the regime $l_e < L < \xi$ [see Fig. 1(a)]. The junction is oriented such that the current flows along the [011] orientation of the underlying crystal structure.

Throughout, we define the $x$ direction as in the plane of the electron gas and parallel to the average current flow, and the $y$ direction as in plane and perpendicular to average current flow. The inset in Fig. 1(a) shows the corresponding components of the applied magnetic field $\mathbf{B}$. To avoid effects of hysteresis as a function of $I$ [42] and $B_z$ [43], measurements as in Fig. 1(c) were obtained by merging the four quadrants separated by

---

[1] An effective mass of $m_\mathrm{eff} = 0.05 m_e$ is estimated from $\mathrm{k \cdot p}$ calculations.

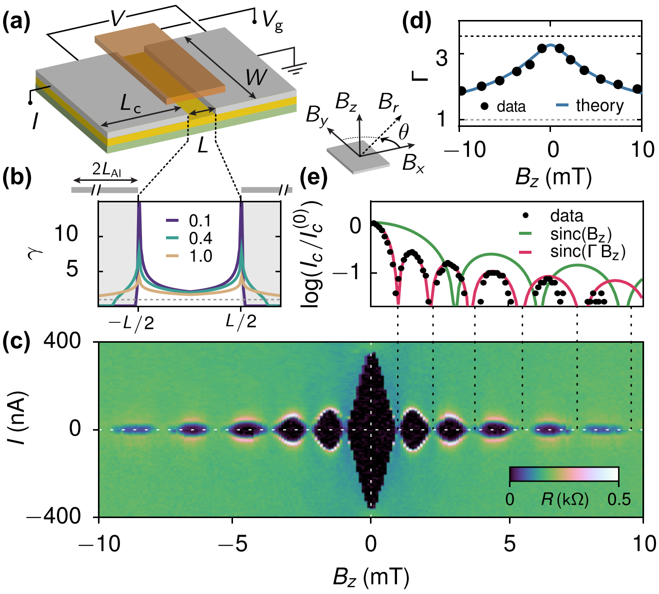

FIG. 1. (a) Device and measurement schematic illustrating the extended superconducting Al banks (gray), InAs quantum well (yellow), and InGaAs barrier (green). The top gate (orange) is shown suspended above the junction, for clarity we have omitted the intervening ALD layer. $L$ and $W$ denote the junction length and width respectively. $L_c$ indicates the physical aluminum contact length. The coordinate system is illustrated in the inset. (b) Local magnetic-field focusing parameter $\gamma$ as a function of position $x$ for three different ratios $\beta = B_z/B_f$. On the upper horizontal axis we highlight $2L_{\mathrm{Al}}$, the contact length entering the model. (c) Differential resistance $R$, as a function of bias current $I$ and perpendicular magnetic field $B_z$. (d) Total magnetic field enhancement in the junction $\Gamma$ as a function of $B_z$, calculated by extraction of the nodes visible in (c,e) (markers), and a fit using Eqs. (3) to (6) (solid line). (e) Critical current $I_c$, plotted logarithmically to highlight periodicity, extracted from (c) (markers). Overlaid are the expectation of Eq. (1) (green) and the modified form taking into account field enhancement due to flux focusing (red).

white dashed lines, each taken separately by sweeping current and field away from zero.

## III. PERPENDICULAR MAGNETIC FIELD

Sweeping the bias current $I$ over a range of perpendicular magnetic fields $B_z$ while measuring the differential resistance $R$ results in the interference pattern shown in Fig. 1(c). This pattern deviates from the expected Fraunhofer form predicted by Eq. (1). For instance, from Eq. (1), we expect equally spaced nodes of the critical current, at values of perpendicular field $B_z = n\Phi_0/(WL)$, where integer numbers of flux quanta penetrate the semiconductor region. Experimentally, we find a deviation from this uniform node spacing, as can be seen from the vertical dashed lines in Fig. 1(c).

In order to investigate this variable node spacing in more detail, we plot in Fig. 1(e) the critical current extracted from Fig. 1(c) as a function of $B_z$ (markers). For reference, we also show the expected Fraunhofer pattern (green) using the lithographic device area, for which $\Phi_0/(WL) = 3.1$ mT. From the data, we find a central lobe half-width of 0.97 mT and a reduced spacing of the subsequent side-lobes, gradually increasing and reaching 1.9 mT for the fifth side-lobe.[2]

To quantify the deviation from the expected uniform spacing, we introduce a dimensionless factor $\Gamma$, the ratio of the expected node position to the observed node position,

$$\Gamma\big(B_z^{(n)}\big) = \frac{n\Phi_0}{B_z^{(n)}LW}, \tag{2}$$

where $B_z^{(n)}$ is the perpendicular magnetic field at node number $n$. A regular Fraunhofer pattern has $\Gamma = 1$ everywhere, as indicated in Fig. 1(d). At low fields, we find $\Gamma \sim 3$. As $B_z$ increases, $\Gamma$ decreases, approaching unity at high fields. The black dots in Fig. 1(d) show the extracted $\Gamma$ based on the data of Fig. 1(c).

The deviation from Eq. (1) leading to $\Gamma > 1$ can be understood as resulting from field-dependent flux focusing from the superconducting contacts. The qualitative behavior of $\Gamma$ is consistent with the superconducting leads passing from a Meissner state at low field, through a mixed state, towards a fully flux-penetrated state above 10 mT. In the Meissner state, the contacts completely expel flux, causing the field in the junction region to be enhanced. When the magnetic field is increased, the thin aluminum banks are slowly pushed into a mixed state as they are penetrated by field lines, leading to a smaller field enhancement in the junction and correspondingly a decreasing $\Gamma$. At high field, the banks are presumably fully penetrated by the incident flux, approaching a negligible field enhancement and $\Gamma \approx 1$.

Previous studies using thick niobium contacts also found large field enhancements in SNS junctions [44,45]. In those studies, however, the leads remained in a full Meissner regime for the perpendicular field range studied, resulting in a constant field enhancement. Because the Al electrodes in the present system are operated close to their critical field $B_c$, the degree of flux focusing depends on field.

To examine the flux-focusing picture more quantitatively, we model the field profile inside the junction following Ref. [46] (see also Ref. [43]). The effective field near a single thin superconducting strip of length $2L_{\mathrm{Al}}$ and infinite width [see Fig. 1(b)], subject to a perpendicular applied field, is given by

$$B_{\mathrm{eff}}(\tilde{x}) = B_f \ln\left(\frac{|\tilde{x}|\sqrt{L_{\mathrm{Al}}^2 - a^2} + L_{\mathrm{Al}}\sqrt{\tilde{x}^2 - a^2}}{a\sqrt{\left|\tilde{x}^2 - L_{\mathrm{Al}}^2\right|}}\right), \tag{3}$$

for $|\tilde{x}| > a$ and $B_{\mathrm{eff}}(\tilde{x}) = 0$ for $|\tilde{x}| \leqslant a$. The coordinate $\tilde{x}$ is the in-plane coordinate perpendicular to the edges of the film, with $\tilde{x} = 0$ corresponding to the center of the film. The length $2a$ corresponds to the extent of a region centered at $\tilde{x} = 0$ where the field is fully expelled due to Meissner screening; this length is given by $a = L_{\mathrm{Al}}/\cosh(B_z/B_f)$, with $B_z$ the

---

[2] The deviation at high field between our result and the expectation is presumably due to an underestimation of the junction area due to the neglect of the finite penetration depth in the leads [63]. Utilizing an effective length $L_{\mathrm{eff}} = L + 2\lambda_L$ (with $\lambda_L$ estimated in Appendix A) yields an expected node spacing of 1.7 mT.

applied perpendicular magnetic field[3] and $B_f$ a characteristic field scale roughly corresponding to the field of first vortex penetration. To account for the finite width of our junction, we argue that $2L_{\mathrm{Al}}$ in this case corresponds not to the physical contact length $L_c$ [see Fig. 1(a)], on the order of 10 $\mu$m, but to an effective length over which flux is focused into the junction. Flux lines further away than $\sim W$ from the junction edge are more likely to be expelled towards the sides rather than into the junction region. We thus use $W$ as a cutoff for the effective contact length and set $L_{\mathrm{Al}} = W$.

To account for both contacts in our SNS geometry, we approximate the total effective perpendicular field profile as

$$B_{\mathrm{tot}}(x) = B_{\mathrm{eff}}(L_{\mathrm{Al}} + L/2 - |x|), \tag{4}$$

expressed in terms of the $x$ coordinate with $x = 0$ corresponding to the center of the SNS junction. We thus make the simplification that the focusing in the junction is dominated by the left (right) contact for negative (positive) $x$. We then use Eqs. (3) and (4) to define a local field enhancement parameter

$$\gamma(\beta,x) = B_{\mathrm{tot}}(x)/B_z, \tag{5}$$

which is a function of the ratio $\beta = B_z/B_f$. In Fig. 1(b), we plot $\gamma$ for three different $\beta$, illustrating the inhomogeneous field profile induced by the superconducting leads. The dashed line in Fig. 1(b) highlights the expectation in the absence of focusing ($\gamma = 1$). Near zero applied field (blue line), the local enhancement peaks strongly close to the superconducting banks. Inside of the superconducting contacts, however, $\gamma$ abruptly falls to zero. When the field is increased (cyan and gold lines) we see a gradual smoothing of the enhancement profile as more of the flux penetrates the superconducting banks.

Integrating Eq. (5) over the junction length allows us to calculate the total field enhancement,

$$\Gamma(B_z) = \frac{1}{L}\int_{-L/2}^{L/2} \gamma(\beta,x)\,dx. \tag{6}$$

We fit the data using Eq. (6) with $B_f$ as the only free parameter. The resulting fit is shown as the blue line in Fig. 1(d), yielding $B_f = 8.2$ mT. This is in good agreement with an estimate for the field of first vortex penetration of the film $B_{c1} = 7.7$ mT (see Appendix A). Besides, detailed calculations for a finite-width geometry predict a low-field enhancement of $\Gamma = (2W/L)^{2/3} \sim 3.5$ as shown by the black dashed line in Fig. 1(d) [47]. The good agreement between this low-field prediction and our model further supports our approximation $L_{\mathrm{Al}} = W$. The resulting continuous function $\Gamma(B_z)$ can then be used to plot the full interference pattern of $I_c(B_z)$, corrected for the flux focusing due to the presence of the superconducting contacts. The resulting $I_c(B_z)$ is plotted in red in Fig. 1(e), and shows excellent agreement with the $I_c(B_z)$ extracted from Fig. 1(c).

Despite its simplicity, our model captures the observed deviations from a regular Fraunhofer pattern in the interference pattern of critical currents, strongly suggesting that the observed aperiodic node spacings are indeed caused by flux focusing in the mixed state of the superconducting leads where $B_z \sim B_{c1}$. As a control experiment we have also studied a device of nominally identical dimensions, but with large flux holes located behind the superconducting contacts. Consistent with our interpretation, negligible field enhancement is observed in this device, independent of the applied field (see Ref. [39] for details).

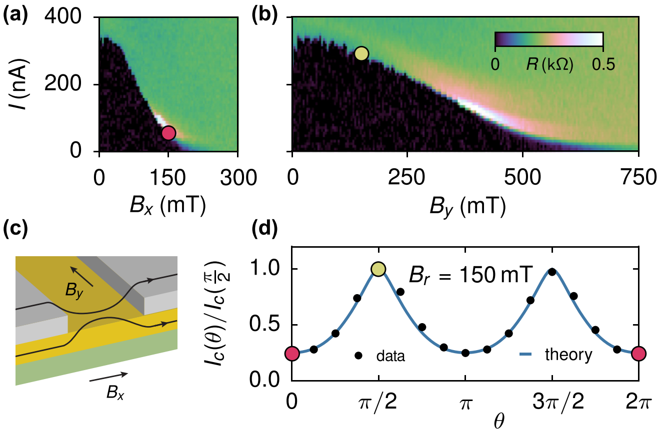

FIG. 2. (a) Differential resistance $R$ as a function of bias current $I$ and in-plane magnetic field $B_x$, applied in the $x$ direction (along the direction of current flow). (b) As in (a) but with the in-plane field $B_y$ along the $y$ direction. (c) Schematic indicating how an in-plane field along $\hat{x}$ can result in an effective flux dipole in the normal region. (d) Normalized critical current $I_c$ as a function of the angle $\theta$ between the in-plane field and $\hat{x}$; the field has a fixed magnitude of $B_r = 150$ mT. The dots represent the experimental data, the solid line is a theory curve based on a one-parameter fit of $\alpha$ at $\theta = \pi$, using the model based on Eq. (7) (see below). The red and yellow markers highlight the correspondence with (a) and (b), respectively.

## IV. IN-PLANE MAGNETIC FIELD

We next examine the effects of in-plane magnetic field on the SNS junction, initially without perpendicular field, $B_z = 0$. Differential resistance as a function of bias current and field magnitude is shown in Fig. 2 for two field orientations: field parallel to the current [$x$ direction, Fig. 2(a)] and field perpendicular to the current [$y$ direction, Fig. 2(b)]. We see that the critical current exhibits a strong anisotropy. The critical field (where the supercurrent becomes fully suppressed) changes from $\sim$200 mT for $\mathbf{B} \parallel \hat{x}$ to $\sim$650 mT for $\mathbf{B} \parallel \hat{y}$. In Fig. 2(d), we show the full dependence of $I_c$ on the direction of the in-plane field, where we fixed the magnitude of the field to $B_r = 150$ mT and $\theta$ denotes the angle between $\mathbf{B}$ and the $x$ direction.

We propose to interpret this anisotropy again in terms of flux focusing due to the Meissner effect. Indeed, also an in-plane field could give rise to flux focusing, since the thickness of the Al layer ($d \sim 10$ nm) is comparable to the London penetration depth of Al, $\lambda_{\mathrm{L}} = 16$ nm [48].

One consequence of the in-plane Meissner effect would be that the density of flux lines just below the aluminum contacts increases, leading to local enhancements of the effective field inside the QW. However, this focusing effect is not expected to

---

[3] For $B_z > B_f$, $B_{\mathrm{eff}}(\tilde{x})$ depends approximately linearly on $B_z$. Indeed, for large $\tilde{x}$, we find $B_{\mathrm{eff}}(\tilde{x}) = B_f \ln\{\cosh(B_z/B_f)[1 + \tanh(B_z/B_f)]\} = B_z$.

depend strongly on the direction of the in-plane field. Another possible effect is that the bending of the field lines around the edges of the contacts may induce a flux dipole in the junction, as exaggerated schematically in Fig. 2(c). Assuming that $\mathbf{B} \parallel \hat{x}$, we see that close to the left contact there is a small component of flux inside the well in the positive $z$ direction, and close to the right contact there is a comparable component in the opposite direction. This flux dipole couples to the in-plane motion of the electrons and can therefore have a strong effect on the interference pattern of $I_c$. Furthermore, the effect is proportional to $B_x$ only, and can thus lead to an anisotropy of $I_c$ in the in-plane field direction.

For $\mathbf{B} \parallel \hat{y}$, the suppression of the critical current with field appears to be fully accounted for by Zeeman effects only. Neglecting orbital effects, an estimate of the magnitude of the effective $g$ factor in the InAs QW from the critical field $B_{y,c}$ yields $|g^*| = 2\Delta^*/\mu_B B_{y,c} \sim 10$, which is in good agreement with previous measurements [14].

As soon as we let the in-plane field deviate from the $y$ direction, a flux dipole will be induced in the N region. The effect of this dipole is most easily understood within a semiclassical picture, where supercurrent arises from coherent transport of Andreev pairs between S regions along well-defined trajectories through the N region. A finite flux dipole makes the phase picked up along a trajectory depend explicitly on the angle $\vartheta$ between the trajectory and the $x$ axis. The dipole will therefore lead to a dephasing of contributions to the current arising from trajectories with different $\vartheta$, and will thus suppress the supercurrent.

We develop a simple but quantitative model of supercurrent through an SNS junction in the presence of a flux dipole by assuming that the junction is ballistic and we can use a semiclassical approximation (where the Fermi wavelength is the smallest length scale in the problem). In the absence of a perpendicular field (or for finite but small $B_z$) we can associate the Andreev bound states in the normal region with straight trajectories connecting the two proximitized regions in the QW. For the energy of such a bound state as a function of $\vartheta$ and the average $y$ coordinate $y_0$ one finds in the limit of $W,L \ll \xi$

$$E(y_0,\vartheta) = \pm\Delta^* \cos\left(\frac{\varphi}{2} - \pi\frac{\Phi}{\Phi_0}\frac{y_0}{W} - \pi\alpha\tan\vartheta\right), \qquad (7)$$

where $\varphi$ is the phase difference between the two proximitized regions, $\Phi$ is the homogeneous flux associated with $B_z$, and $\alpha = \alpha_0\cos\theta$ depends on $B_x$ and parametrizes the effect of flux focusing.[4] The contribution of all Andreev bound states to the free energy $F$ of the junction is found by summing (7) over all allowed $y_0$ and $\vartheta$, weighted by a Fermi function. The supercurrent then follows as $I_s(\varphi) = (2e/\hbar)\partial F/\partial\varphi$ and the critical current is simply $I_c = \max_\varphi I_s(\varphi)$.

We convert the sums over $y_0$ and $\vartheta$ into integrals and, assuming for simplicity zero temperature and fully absorbing sides at $y = \pm W/2$, we numerically compute the critical current for $\Phi = 0$ as a function of the in-plane field direction $\theta$. Comparing the resulting $I_c(\theta)/I_c(\pi/2)$ with the data shown in Fig. 2(d) results in a single-parameter fit yielding $\alpha_0 = 0.32 \pm 0.01$. The resulting fit is shown as the solid blue line in the figure and shows excellent agreement with the data. We can also try to connect this numerical value for $\alpha_0$ to our device geometry. A rough estimate for $\alpha_0$ in terms of device parameters is $\alpha_0 = \eta B_r W d_f/\Phi_0$, where $d_f$ is the width of the strips close to the proximitized regions where flux focusing is significant and $\eta$ is the fraction of $B_x$ that locally contributes to magnetic flux oriented along $\pm\hat{z}$. We thus estimate that there is only a significant out-of-plane flux in two narrow strips of area $W \times d_f$ bordering the proximitized regions, and $0 \leqslant \eta \leqslant 1$ is a phenomenological parameter related to the average degree of bending of the flux lines. (For instance, $\eta = 1/\sqrt{2}$ would correspond to a situation where the flux lines make on average an angle of 45° with the plane of the junction within two strips of width $d_f$.) If we estimate $d_f = d = 10$ nm, we find for $B_r = 150$ mT and $\alpha_0 = 0.32$ that $\eta = 0.29$, corresponding to an average local out-of-plane angle of $\sim$20°.

## V. COMBINED PERPENDICULAR AND IN-PLANE MAGNETIC FIELDS

Sweeping $B_z$ while still applying an in-plane field we observe two new and striking effects, as shown in Figs. 3(a)

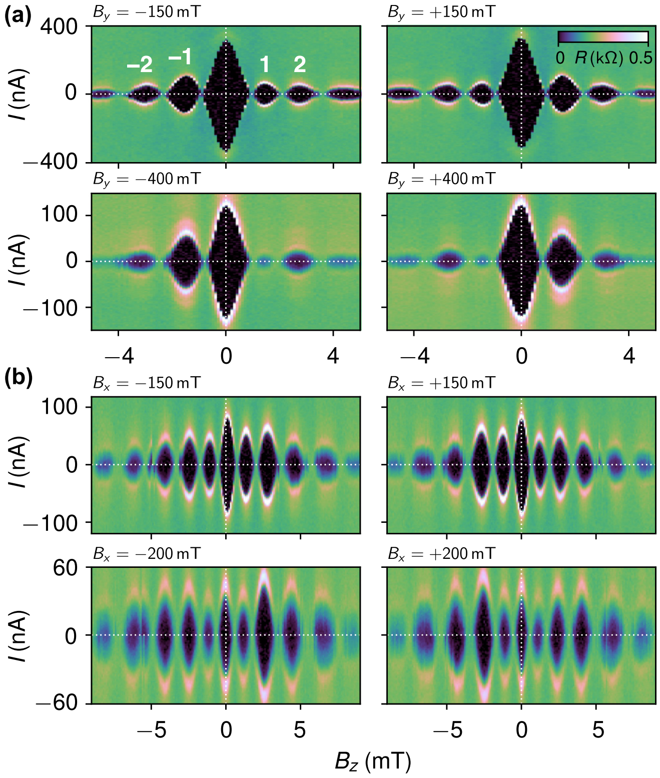

FIG. 3. (a) Differential resistance $R$ as a function of bias current $I$ and $B_z$, measured for different values of fixed $B_y$: $B_y = \pm150$ mT (top) and $B_y = \pm400$ mT (bottom). The white numbers in the upper left panel indicate the lobe indices. (b) As (a), for an in-plane magnetic field applied along $\hat{x}$, using $B_x = \pm150$ mT (top) and $B_x = \pm200$ mT (bottom).

---

[4] We note that this model neglects the effect of SOI. We have verified that spin-orbit effects, calculated along the lines of Ref. [23], yield changes on the order of a few percent while the experimental anisotropy is of the order 1.

and 3(b). First, in the presence of an in-plane field, the critical current develops a pronounced asymmetry between positive and negative $B_z$; we observe this for all directions of in-plane field. Second, increasing the in-plane field when directed along $\hat{x}$ results in (i) a decrease of the zero-perpendicular-field critical current, $I_c^{(0)}$; (ii) a relative enhancement of all side-lobe maxima as compared to the central one, approaching a situation where all observable maxima are roughly equal; (iii) a gradual decrease of the width of the central lobe. We initially focus on the latter effects, associated with $B_x$, and discuss the asymmetries in Sec. V B.

### A. SNS-to-SQUID transition

Both the narrowing of the central lobe and the gradual equalizing of lobe maxima with increasing $B_x$ can be understood as resulting from the flux-focusing mechanism discussed in the previous section. As argued above, a large $B_x$ could lead to a situation where the supercurrent in the center of the junction is suppressed and most transport takes place along the edges of the normal region, making the system more like a SQUID, with conduction only along sample edges, instead of a planar SNS junction with uniform current flow. In the pure-SQUID limit, one expects for the critical current $I_c(\Phi) \propto |\cos(\pi\Phi/\Phi_0)|$ instead of a Fraunhofer-like pattern, i.e., all lobes will have the same maximum value and the same width $\Phi_0$. This is qualitatively consistent with the trend we observe in Fig. 3(b).

To further examine the picture of a focusing-induced flux dipole leading to SQUID-like current flow, we use the model from Sec. IV to calculate the critical current as a function of $\Phi = B_z LW$ for different focusing parameters $\alpha$, and compare the resulting theoretical interference patterns $I_c(B_z)$ with experimental data.[5] In Fig. 4(a), the calculated $I_c(B_z)$ is plotted for five values of $\alpha$, corresponding to $B_x = 0$, 100, 150, 200, and 300 mT (assuming for simplicity a linear relation between $\alpha$ and $B_x$, and setting $\alpha = 0.32$ for $B_x = 150$ mT). These numerical results reproduce the two main features discussed above. (i) As highlighted by the vertical gray dashed lines, the width of the central lobe decreases with increasing $B_x$. For $B_x = 0$ we find a width of roughly $2.6\Phi_0$ (slightly larger than the $2\Phi_0$, corresponding to a regular Fraunhofer pattern, presumably due to finite size effects[6]), and for large $B_x$ it approaches $\Phi_0$, the SQUID limit. (ii) The heights of all side-lobes in Fig. 4(a) increase relative to the central lobe when increasing $B_x$, approaching a situation where all lobes are of comparable height. Both these trends are qualitatively consistent with the experimental observations and support our interpretation in terms of a focusing-induced flux dipole.

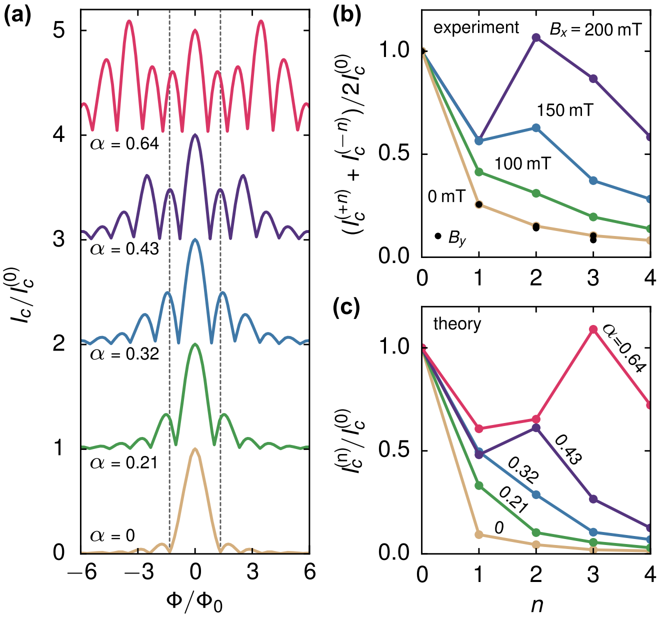

FIG. 4. (a) Numerically calculated critical current as a function of $\Phi$, normalized by $I_c^{(0)}$. The in-plane field is assumed along $\hat{x}$ and the different curves correspond to $\alpha = 0$, 0.21, 0.32, 0.43, and 0.64, from bottom to top (each offset by 1). (b) Symmetrized side-lobe maxima extracted from experimental data, for different in-plane fields. The field magnitudes indicated in the plot refer to $\mathbf{B} \parallel \hat{x}$; all data points for $\mathbf{B} \parallel \hat{y}$ (black dots) fall on top of the set marked 0 mT. (c) Side-lobe maxima obtained from the numerical data shown in (a).

We next examine the behavior of the sequence of side-lobe maxima for different $B_x$ in more detail. In Fig. 4(b), we show the experimentally obtained maxima for four different $B_x$, where we removed the complicating asymmetry in $\pm B_z$ (considered in detail below) by symmetrizing and normalizing the data, $(I_c^{(+n)} + I_c^{(-n)})/2I_c^{(0)}$, using side-lobe numbers $n$ as indicated in the top left pane of Fig. 3(a). When $B_x$ is increased, we see that (i) the side-lobe maxima are enhanced relative to the central peak, and (ii) the sequence of maxima $I_c^{(n)}$ becomes nonmonotonic, even yielding side-lobes that exceed the central lobe in magnitude at the highest field ($B_x = 200$ mT). We can extract the same data from the numerical results presented in Fig. 4(a), and show in Fig. 4(c), the resulting lobe maxima $I_c^{(n)}$, normalized by $I_c^{(0)}$. Comparing with the experimental data, we see that the model not only reproduces the gradual enhancement of the side-lobe maxima for increasing $B_x$, but also captures the more detailed behavior of the series of side-lobes. Whereas at small $B_x$ the maxima $I_c^{(n)}$ monotonically drop for increasing $|n|$, at larger $B_x$ the series becomes nonmonotonic, ultimately even producing interference patterns where side-lobes exceed the central maximum in height.

The black dots in Fig. 4(b), all falling on top of the yellow curve corresponding to $B_x = 0$, represent two data sets with the side-lobe maxima for $B_y = 150$ and 300 mT (all at $B_x = 0$), where we removed the asymmetry by symmetrizing $I_c$ in $\pm B_z$ (as above, this data is normalized by $I_c^{(0)}$). The fact that all

---

[5] In this section, we concentrate largely on qualitative features and thus for simplicity neglect the effect of out-of-plane focusing as discussed in Sec. III.

[6] Close to the edges of the junction, where $y_0 \approx \pm W/2$, there are fewer angles $\vartheta$ available to construct Andreev bound states with. Consequently, the flux penetrating the N region close to the edges has less influence on the total average supercurrent through the junction than the flux penetrating the center of the region. To achieve the first full suppression of the supercurrent by perfect destructive interference of all trajectories, one thus needs to go to slightly higher fields than $B_z = \Phi_0/(WL)$.

these data are equal to the data without in-plane field, within experimental accuracy, confirms that the qualitative change of the interference pattern that we attribute to an SNS-to-SQUID transition only depends on $B_x$. It also suggests that the asymmetry in $\pm B_z$ has a physical origin which is distinct from the focusing effects discussed in this section.

In conclusion, the model presented in Sec. IV, which assumes a simple flux dipole in the normal region proportional to $B_x$, appears to capture many aspects of the qualitative behavior of $I_c(B_z)$ as a function of in-plane field. All global trends we observe in the data are reproduced by our numerical calculations, indicating a transition from Fraunhofer-like interference at zero in-plane field to SQUID-like behavior in the presence of sufficiently strong $B_x$. A flux dipole in the normal region, induced by flux focusing of the $x$ component of the in-plane field thus appears to provide the likely explanation for our observations. However, we emphasize that the model used in this section is *not* capable of generating the striking asymmetries in $\pm B_z$.

### B. Asymmetries in the interference patterns

Finally, we turn our attention to the surprising asymmetries observed in the interference patterns of Figs. 3(a) and 3(b). To quantify the asymmetry, we define an asymmetry parameter $\mathcal{A}_n$ for each side-lobe pair $\{n, -n\}$ as

$$\mathcal{A}_n = \frac{I_c^{(-n)} - I_c^{(n)}}{I_c^{(-n)} + I_c^{(n)}}, \tag{8}$$

which yields the relative difference in the side-lobe maxima for $\pm B_z$. In this section, we will investigate systematic dependencies of $\mathcal{A}_n$ on the magnitude $B_r$ and direction $\theta$ of the in-plane field.

In Fig. 5(a), we plot $\mathcal{A}_1$ (blue) and $\mathcal{A}_2$ (red) as functions of $B_r$ with the field applied along $\hat{y}$. The asymmetry of the first node $\mathcal{A}_1$ is seen to scale roughly linearly with $B_r$, reaching ~100% at the highest fields, while the asymmetry of the second node $\mathcal{A}_2$ remains zero within experimental uncertainty. In Fig. 5(b), for in-plane field now along $\hat{x}$, we now see that both $\mathcal{A}_1$ and $\mathcal{A}_2$ increase proportionally to $B_r$, both reaching ~25% at 250 mT, just before $I_c$ gets fully suppressed (see Fig. 2). All asymmetries thus seem to scale linearly with the magnitude of the applied in-plane field. The slope of $\mathcal{A}_n(B_r)$, however, varies considerably: from positive, to zero, to negative for different $n$ and $\theta$. From these two angles ($\theta = 0$ and $\theta = \pi/2$) no systematics are evident.

The dependence of the $\mathcal{A}_n$ on the direction of the in-plane field is shown in Fig. 5(c). We plot the measured absolute asymmetries $|\mathcal{A}_1|$ and $|\mathcal{A}_2|$ for 16 angles at a fixed field magnitude $B_r = 150$ mT (we use solid and dashed connectors to indicate where the obtained $\mathcal{A}_n$ are positive and negative, respectively). As a reference, we include the anisotropic angular dependence of $I_c^{(0)}$ (filled gray area, plotted in arbitrary units), which we analyzed in terms of a Meissner-induced flux dipole in Sec. IV. The observed evolution of the asymmetry as a function of $\theta$ in the present sample has a number of interesting characteristics: (i) the asymmetry of the first side-lobe is maximal for $\theta \sim 5\pi/8$ and minimal in the perpendicular direction $\theta \sim \pi/8$. (ii) The maximal and minimal asymmetries of the second lobe are roughly perpendicular to those of the first lobe. (iii) Consistent with the mirroring in $B_z$ observed upon inversion of $B_x$ or $B_y$ (see Fig. 3), both asymmetries have a well defined node at zero about which the behavior of $\mathcal{A}_n$ is antisymmetric in $\theta$ (or equivalently $B_r$).

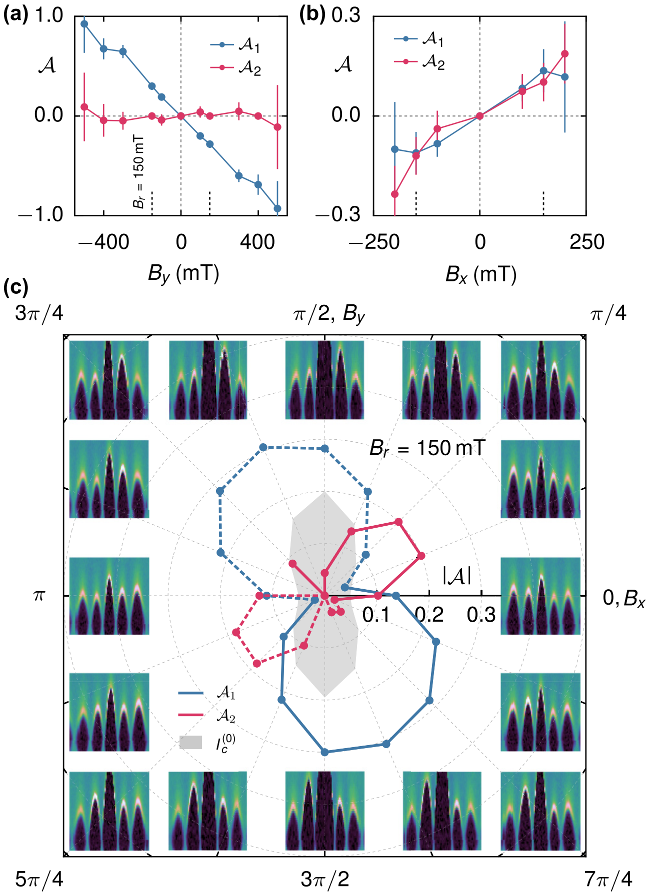

FIG. 5. (a) Normalized asymmetry $\mathcal{A}$ in the lobe maxima as a function of $B_y$, for the first two side-lobes (shown in blue and red respectively). (b) As (a), for magnetic fields oriented along $\hat{x}$. (c) Magnitude of the asymmetry parameter $|\mathcal{A}|$ as a function of in-plane field angle $\theta$. Solid(dashed) lines connect points indicating where $\mathcal{A}_n$ are positive(negative). The in-plane field is fixed to $B_r = 150$ mT. To emphasize the deviation of this angular dependence from the anisotropy observed for $B_z = 0$ (see Sec. IV), we include in gray the height of the central lobe $I_c^{(0)}$ as a function of $\theta$ (arbitrary units). The panels along the edges show the differential-resistance data from which the asymmetries are extracted.

Separate samples have demonstrated similar behavior, including a linear scaling of the $\mathcal{A}_n$ in field magnitude and a continuous angular evolution of the asymmetry antisymmetric upon $\pi$ rotation.[7] Many of the details, however, are very different from sample to sample: The observed magnitudes of $\mathcal{A}_1$ and $\mathcal{A}_2$ for given $B_r$ fluctuate up to 100%, and also the angular alignment of their minima and maxima varies across different samples (also the roughly perpendicular orientation of the maxima of $\mathcal{A}_1$ and $\mathcal{A}_2$ observed in Fig. 5 is not a consistently observed feature). The variation of all these details does not display a clear trend following any of the controllable

---

[7] See Ref. [39] for more details and data from different samples.

device parameters, such as $W$, $L$, or the orientation of the junction with respect to the crystallographic axes of the InAs wafer. This suggests that the asymmetries are the result of an intricate interplay of many device-dependent factors, most likely including SOI, disorder, local details of the coupling between the InAs and the Al, and the microscopic shape of the sample.

Although it thus seems difficult to pinpoint the physical mechanism responsible for the asymmetries, we can try to develop a qualitative picture by carrying out a general analysis along the lines of Ref. [49]. We construct a model (Bogoliubov-de Gennes) Hamiltonian, treating the electrons in the junction as a two-dimensional free electron gas in the presence of a vector potential due to the applied magnetic field (including the flux dipole proportional to $B_x$). We add to this Hamiltonian finite superconducting pairing potentials of equal magnitude under the left and right contacts, and terms accounting for Rashba and Dresselhaus SOI, Zeeman splitting, and an arbitrary disorder potential $V(x,y)$. We can then investigate under what circumstances the symmetries of the total Hamiltonian dictate the critical current to be symmetric in $B_z$ and when this symmetry is broken (see Ref. [39] for details).

The most important conclusion is that if $V(x,y) = 0$ the symmetry $I_c(+B_z) = I_c(-B_z)$ is protected, and the model will produce a symmetric interference pattern for a symmetrically shaped sample, no matter how all other parameters are tuned. Disorder or other spatial asymmetries in the junction are thus a necessary ingredient for obtaining an asymmetric critical current. More specifically, we find that (i) in the presence of an in-plane field oriented along $\hat{x}$, only one of the mirror asymmetries $V(x,y) \neq V(-x,y)$ or $V(x,y) \neq V(x,-y)$ has to be present to allow for an asymmetric interference pattern. (ii) If the in-plane field is along $\hat{y}$, a direction along which we observe a strong asymmetry (see Fig. 5), only $V(x,y) \neq V(x,-y)$ breaks the symmetry.

As a side note, we mention that some combinations of symmetry-breaking ingredients only affect the higher Fourier components of the current-phase relation $I_s(\varphi)$. For instance, in order to have $I_c(+B_z) \neq I_c(-B_z)$ in combination with a purely sinusoidal $I_s(\varphi)$, it is required to have (in addition to disorder): (i) a finite $B_x$ or (ii) a finite $B_y$ *and* SOI. In this case, the degree of asymmetry left at $\theta = \pi/2$ could thus present a measure for the strength of SOI in the junction. In our experiment, however, current was controlled rather than phase, so we do not know to what degree the current-phase relation is nonsinusoidal. In general, one expects junctions with weak NS-coupling to have a nearly sinusoidal $I_s(\varphi)$ [50]. Engineering a barrier between the normal and proximitized regions in the QW could thus present a way to obtain more detailed knowledge about the SOI in the sample.

Our qualitative analysis thus clearly supports the idea that a key role is played by structural asymmetries in the device, already suggested by the strong sample-to-sample variation observed in the data. As to the mechanisms that can break spatial symmetries in our samples, we identify three: (i) spatial variation in the couplings to the superconducting contacts, (ii) imperfections in the microscopic shape of the junction, or (iii) a random disorder potential. Owing to the epitaxial growth of Al and the small size of the junction, we expect the couplings to the contacts to be relatively homogeneous. Further, measurements of the asymmetry as a function of gate voltage, presented in Appendix B, show that the asymmetries in $I_c$ are robust to gating in both magnitude and angular dependence. This weak gate dependence could indicate that the dominant spatial symmetry breaking mechanism is stable, which also suggests that it is either the specific shape of the junction or a fixed disorder potential induced by ionized impurities in the QW. To further support this picture, we also performed tight-binding numerical simulations of the supercurrent through a two-dimensional disordered SNS junction focusing on the asymmetry parameters $\mathcal{A}_n$; the results are presented in the Supplemental Material. We find patterns that look similar to those extracted from the experimental data and also display a strong variation from device to device (i.e., when we change the disorder configuration). This also supports our speculation that disorder plays a crucial role in the underlying mechanisms responsible for the asymmetries.

An alternative explanation of the asymmetries one could propose is in terms of Abrikosov vortices near the junction; the presence of such vortices is known to induce asymmetries in the critical current upon inversion of $B_z$. In the limit of single vortices the behavior is well understood and studies have successfully mapped the position of vortices from the modification of interference patterns [32,51]. For large numbers of vortices, experimental and theoretical investigations exist in the limit of disordered vortex arrays [52,53], yielding seemingly random interference patterns. Theoretical work on ordered vortex arrays predicts symmetric interference patterns described by minor modifications to Eq. (1) [54].

While we expect flux penetration of the leads in a perpendicular field, and thus vortices to be present, we observe no indication of quantized vortex entrance events, i.e., sudden switches in the critical current [51]. Furthermore, we do not observe asymmetries without the application of an in-plane field, which seems to be incompatible with vortices as the origin of the asymmetry. Finally, the mirror symmetry in $B_z$ of the observed asymmetry upon reversing the sign of the in-plane field would require an almost perfect reversal of the vortex configuration, which is highly unlikely.

To conclude, we believe that in the mechanisms underlying the asymmetries we explored in this section, an important role is being played by structural disorder in the samples. Given the complexity of the system and the randomness of what appears to be the most important symmetry-breaking ingredient, it is currently unclear whether measurements of the asymmetry could be used to quantify the strengths of SOI and Zeeman coupling in these devices. SNS junctions designed with a well-defined built-in dominant asymmetry might allow for disentangling these effects; this warrants further work.

## VI. CONCLUSION

We report a systematic experimental study of the behavior of two-dimensional epitaxial Al/InAs/Al SNS junctions under the application of out-of-plane as well as in-plane magnetic fields. Our system is of great interest since it combines strong spin-orbit interaction with exceptionally good semiconductor-superconductor coupling and, due to the epitaxially grown superconductor, it can withstand large in-plane magnetic fields. Measuring the critical current as a function of the magnitude and direction of the applied magnetic field, we discover a strong influence on the properties of the junction of flux focusing from the superconducting contacts, both for perpendicular and in-plane magnetic fields. For in-plane fields applied along the direction of average current flow, flux focusing results in an effective flux dipole in the normal region, causing transport to be localized towards the edges of the sample. We thus find that the in-plane field may act as a novel control knob allowing for magnetic confinement of Andreev states in such hybrid superconductor-semiconductor systems. We further observe striking asymmetries in the interference pattern $I_c(\pm B_z)$ when an in-plane field is applied. Although most qualitative properties of these asymmetries remain unexplained, we argue that the microscopic structure of the device plays an crucial role, potentially masking the influences of spin-orbit and Zeeman coupling.

## ACKNOWLEDGMENTS

We thank A. Rasmussen and L. Levitov for valuable discussions. Research was supported by Microsoft Project Q, the Danish National Research Foundation and the National Science Foundation through the National Nanotechnology Infrastructure Network. F.N. acknowledges support from a Marie Curie Fellowship (No. 659653). C.M.M. acknowledges support from the Villum Foundation.

## APPENDIX A: ESTIMATING $\mathbf{B_{c1}}$

In order to determine $B_{c1}$, we need to estimate the parameter $\kappa = \lambda/\xi$. We use values for bulk Al from the literature [55]: $\xi_{\text{bulk}} = 1.6\ \mu\text{m}$ and $T_{c,\text{bulk}} = 1.2$ K. From our measurements we have an accurate value for $T_c$ (see Ref. [39]) and we know from [28] that

$$\Delta(0) = 1.76\, k_B T_c \quad \text{and} \quad \xi = \frac{h v_F}{\pi \Delta}. \tag{A1}$$

These expressions allow us to determine the coherence length in the thin film limit as a function of known parameters, yielding

$$\xi_{\text{thin}} = \xi_{\text{bulk}} \frac{T_{c,\text{bulk}}}{T_{c,\text{thin}}}, \tag{A2}$$

the same method is, e.g., used in Ref. [56]. Substituting the known values of $T_{c,\text{bulk}}$, $\xi_{\text{bulk}}$, and the $T_c = 1.5$ K measured gives $\xi = 1.28\ \mu\text{m}$ for the superconducting film. We may also estimate the penetration depth from known quantities [28,57]:

$$\lambda = \lambda_L(0)\sqrt{1 + \frac{\xi}{d}}. \tag{A3}$$

Using the value for $\lambda_L = \lambda_{L,\text{bulk}} = 16$ nm from the literature and using the modified $\xi$ calculated above, we obtain $\lambda = 180$ nm for a film thickness of $d = 10$ nm.

Finally, we can estimate $B_{c1}$. For type-II superconductors, the field of first vortex penetration (assuming a magnetic field perpendicular to the film) is given by [28]

$$B_{c1} \approx \frac{\Phi_0}{4\pi\lambda^2} \ln\kappa = \frac{B_c}{\sqrt{2}\kappa} \ln\kappa. \tag{A4}$$

Importantly, this formula assumes that $\kappa > 1/\sqrt{2}$. For our values $\kappa \approx 0.2 \times (1/\sqrt{2})$, clearly in the type-I regime. However, in the thin-film limit, the penetration depth is renormalized such that $\kappa = \Lambda/\xi$ [58,59], where $\Lambda \sim \lambda^2/d$. Using this renormalization we obtain $\kappa \sim 2.5$, which lies in the type-II regime. Using these numbers together with $B_{c,z} \sim 30$ mT yields $B_{c1} = 7.7$ mT. It is worth noting that the first vortex may penetrate before $B_{c1}$ is reached [60].

## APPENDIX B: GATE DEPENDENCE

The QW used for the experiment hosts two subbands at $V_g = 0$. Based on Hall measurements, we know that the transition to the single subband limit is achieved at $V_g \sim -2$ V.

Fig. 6(a) shows the measured differential resistance $R$, as a function of gate voltage $V_g$ and bias current $I$. The interference patterns obtained at four different values of $V_g$ are shown in Figs. 6(c)–6(f). From these data, we can extract the field-dependent critical current $I_c(B_z)$, which we correct for the flux focusing parameter $\Gamma$ (see Sec. III). The resulting $I_c(B_z)$ can be used to calculate the supercurrent density $J_c(y)$ using the Dynes and Fulton method [33], the results are shown in the insets in Figs. 6(c)–6(f). All curves show a supercurrent density accumulation towards the lateral edges of the SNS, the effect being more accentuated at negative gate voltages. This effect

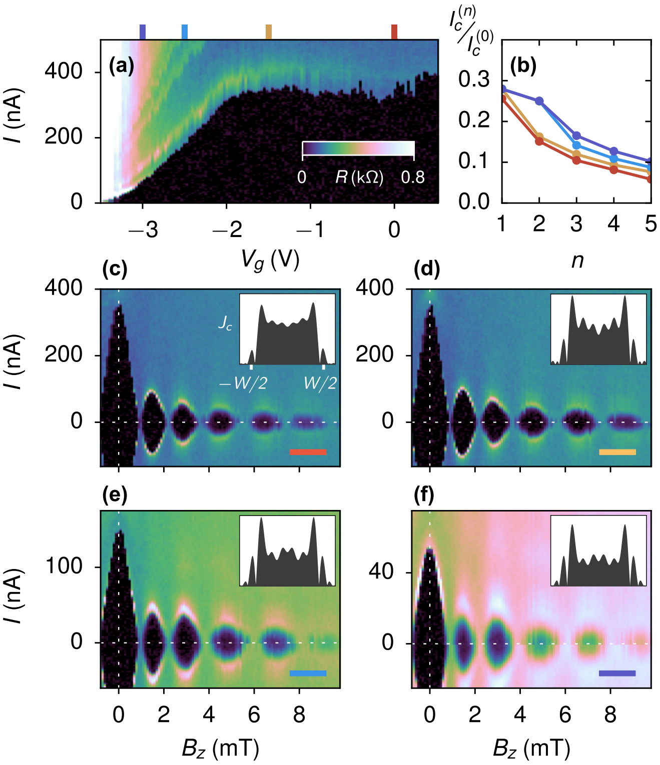

FIG. 6. (a) Differential resistance $R$, as a function of gate voltage $V_g$ and bias current $I$. (b) Normalized critical current as a function of side-lobe index $n$, for varying gate voltages, denoted by the colored markers in (a). (c)–(f) Differential resistance $R$, as a function of bias current $I$ and out-of-plane magnetic field $B_z$, for the different values of gate voltage marked in (a). Insets show the extracted supercurrent density $J_c(y)$. (c) is based on the same data set as shown in Fig. 1(c)

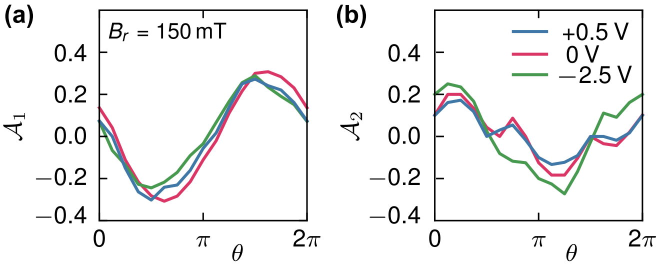

FIG. 7. (a) Measured magnetic field asymmetry $\mathcal{A}_1$ for the first side-lobe as a function of in-plane field angle $\theta$. (b) as (a) for the second side-lobe $\mathcal{A}_2$. Curves are colored according to gate voltage. Note that the zero gate voltage data is the same as that displayed in Fig. 5.

is also captured in Fig. 6(b), where we plot the normalized side-lobe maxima. Compatibly with the accumulation of $J_c$ at the edges, the side-lobe maxima are gradually lifted upon depletion of the 2DEG. For $V_g < -2$ V, an anomalous lifting of the $n = 2$ side-lobe is observed, similar to Fig. 4(b) where in an in-plane field is applied. We interpret the gate-voltage-induced enhancement of the critical current density at the mesa edges with band bending. InAs is well known to host a surface accumulation layer due to the breaking of the translational symmetry of the crystal [61,62]. Due to the presumably high initial electron density at the edges, we expect these features to dominate as the 2DEG is depleted.

Finally, we investigate the effect of the gate on the asymmetries in the interference pattern. In Figs. 7(a) and 7(b), we plot the asymmetry of the first two lobes, $\mathcal{A}_1$ and $\mathcal{A}_2$, respectively, as a function of the in-plane field angle at a fixed magnitude of $B_r = 150$ mT. The asymmetry of the two lobes is largely independent of gate voltage, both in amplitude and angular alignment. These results highlight how the asymmetries are robust against variation of carrier density and the subband occupation of the system.

[1] A. Y. Kitaev, Phys. Usp. **44**, 131 (2001).
[2] J. D. Sau, R. M. Lutchyn, S. Tewari, and S. Das Sarma, Phys. Rev. Lett. **104**, 040502 (2010).
[3] V. Mourik, K. Zuo, S. M. Frolov, S. R. Plissard, E. P. A. M. Bakkers, and L. P. Kouwenhoven, Science **336**, 1003 (2012).
[4] A. Das, Y. Ronen, Y. Most, Y. Oreg, M. Heiblum, and H. Shtrikman, Nat. Phys. **8**, 887 (2012).
[5] M. T. Deng, C. L. Yu, G. Y. Huang, M. Larsson, P. Caroff, and H. Q. Xu, Nano Lett. **12**, 6414 (2012).
[6] H. O. H. Churchill, V. Fatemi, K. Grove-Rasmussen, M. T. Deng, P. Caroff, H. Q. Xu, and C. M. Marcus, Phys. Rev. B **87**, 241401 (2013).
[7] J. Alicea, Y. Oreg, G. Refael, F. von Oppen, and M. P. Fisher, Nat. Phys. **7**, 412 (2011).
[8] J. Nitta, T. Akazaki, H. Takayanagi, and T. Enoki, Phys. Rev. Lett. **78**, 1335 (1997).
[9] J. P. Heida, B. J. van Wees, J. J. Kuipers, T. M. Klapwijk, and G. Borghs, Phys. Rev. B **57**, 11911 (1998).
[10] J. Nitta, Y. Lin, T. Akazaki, and T. Koga, Appl. Phys. Lett. **83**, 4565 (2003).
[11] T. Kawakami and H. Takayanagi, Appl. Phys. Lett. **46**, 92 (1985).
[12] C. Nguyen, J. Werking, H. Kroemer, and E. L. Hu, Appl. Phys. Lett. **57**, 87 (1990).
[13] J. Nitta, T. Akazaki, H. Takayanagi, and K. Arai, Phys. Rev. B **46**, 14286 (1992).
[14] J. Shabani, M. Kjaergaard, H. J. Suominen, Y. Kim, F. Nichele, K. Pakrouski, T. Stankevic, R. M. Lutchyn, P. Krogstrup, R. Feidenhans'l, S. Kraemer, C. Nayak, M. Troyer, C. M. Marcus, and C. J. Palmstrøm, Phys. Rev. B **93**, 155402 (2016).
[15] M. Kjaergaard, F. Nichele, H. J. Suominen, M. P. Nowak, M. Wimmer, A. R. Akhmerov, J. A. Folk, K. Flensberg, J. Shabani, C. J. Palmstrøm, and C. M. Marcus, Nat. Commun. **7**, 12841 (2016).
[16] M. Kjaergaard, H. J. Suominen, M. P. Nowak, A. R. Akhmerov, J. Shabani, C. J. Palmstrøm, F. Nichele, and C. M. Marcus, arXiv:1607.04164.
[17] S. Hart, H. Ren, M. Kosowsky, G. Ben-Shach, P. Leubner, C. Brüne, H. Buhmann, L. W. Molenkamp, B. I. Halperin, and A. Yacoby, Nat. Phys. **13**, 87 (2017).
[18] P. San-Jose, J. Cayao, E. Prada, and R. Aguado, New J. Phys. **15**, 075019 (2013).
[19] P. San-Jose, E. Prada, and R. Aguado, Phys. Rev. Lett. **112**, 137001 (2014).
[20] M. Hell, M. Leijnse, and K. Flensberg, arXiv:1608.08769.
[21] F. Pientka, A. Keselman, E. Berg, A. Yacoby, A. Stern, and B. I. Halperin, arXiv:1609.09482.
[22] J.-F. Liu and K. S. Chan, Phys. Rev. B **82**, 125305 (2010).
[23] E. V. Bezuglyi, A. S. Rozhavsky, I. D. Vagner, and P. Wyder, Phys. Rev. B **66**, 052508 (2002).
[24] B. Béri, J. H. Bardarson, and C. W. J. Beenakker, Phys. Rev. B **77**, 045311 (2008).
[25] A. A. Reynoso, G. Usaj, C. A. Balseiro, D. Feinberg, and M. Avignon, Phys. Rev. Lett. **101**, 107001 (2008).
[26] A. A. Reynoso, G. Usaj, C. A. Balseiro, D. Feinberg, and M. Avignon, Phys. Rev. B **86**, 214519 (2012).
[27] T. Yokoyama, M. Eto, and Y. V. Nazarov, Phys. Rev. B **89**, 195407 (2014).
[28] M. Tinkham, *Introduction to Superconductivity*, 2 ed., Dover Books on Physics (Dover, New York, 2004).
[29] J. M. Rowell, Phys. Rev. Lett. **11**, 200 (1963).
[30] T. Nishino, U. Kawabe, and E. Yamada, Phys. Rev. B **34**, 4857 (1986).
[31] K. Inoue and T. Kawakami, J. Appl. Phys. **65**, 1631 (1989).
[32] S. L. Miller, K. R. Biagi, J. R. Clem, and D. K. Finnemore, Phys. Rev. B **31**, 2684 (1985).
[33] R. C. Dynes and T. A. Fulton, Phys. Rev. B **3**, 3015 (1971).
[34] H.-Y. Hui, A. M. Lobos, J. D. Sau, and S. Das Sarma, Phys. Rev. B **90**, 224517 (2014).
[35] J. H. Lee, G.-H. Lee, J. Park, J. Lee, S.-G. Nam, Y.-S. Shin, J. S. Kim, and H.-J. Lee, Nano Lett. **14**, 5029 (2014).
[36] S. Hart, H. Ren, T. Wagner, P. Leubner, M. Muhlbauer, C. Brune, H. Buhmann, L. W. Molenkamp, and A. Yacoby, Nat. Phys. **10**, 638 (2014).

[37] V. S. Pribiag, A. J. A. Beukman, F. Qu, M. C. Cassidy, C. Charpentier, W. Wegscheider, and L. P. Kouwenhoven, Nat. Nanotechnol. **10**, 593 (2015).

[38] M. T. Allen, O. Shtanko, I. C. Fulga, A. R. Akhmerov, K. Watanabe, T. Taniguchi, P. Jarillo-Herrero, L. S. Levitov, and A. Yacoby, Nat. Phys. **12**, 128 (2015).

[39] See Supplemental Material at http://link.aps.org/supplemental/10.1103/PhysRevB.95.035307 for the detailed wafer structure, characterization of the superconducting Al film, supplementary devices, symmetry analysis, and tight-binding simulations.

[40] P. H. C. Magnée, S. G. den Hartog, B. J. v. Wees, T. M. Klapwijk, W. van de Graaf, and G. Borghs, Appl. Phys. Lett. **67**, 3569 (1995).

[41] T. Schäpers, *Superconductor/Semiconductor Junctions*, Springer Tracts in Modern Physics Vol. 174 (Springer, Berlin, Heidelberg, 2001).

[42] H. Courtois, M. Meschke, J. T. Peltonen, and J. P. Pekola, Phys. Rev. Lett. **101**, 067002 (2008).

[43] E. H. Brandt and M. Indenbom, Phys. Rev. B **48**, 12893 (1993).

[44] Y. Harada, S. Jensen, T. Akazaki, and H. Takayanagi, Physica C: Superconductivity **367**, 229 (2002).

[45] J. Paajaste, M. Amado, S. Roddaro, F. S. Bergeret, D. Ercolani, L. Sorba, and F. Giazotto, Nano Lett. **15**, 1803 (2015).

[46] E. Zeldov, J. R. Clem, M. McElfresh, and M. Darwin, Phys. Rev. B **49**, 9802 (1994).

[47] J. Gu, W. Cha, K. Gamo, and S. Namba, J. Appl. Phys. **50**, 6437 (1979).

[48] I. S. Khukhareva, Sov. Phys. JETP **16**, 828 (1963).

[49] A. Rasmussen, J. Danon, H. Suominen, F. Nichele, M. Kjaergaard, and K. Flensberg, Phys. Rev. B **93**, 155406 (2016).

[50] A. A. Golubov, M. Y. Kupriyanov, and E. Il'ichev, Rev. Mod. Phys. **76**, 411 (2004).

[51] T. Golod, A. Rydh, and V. M. Krasnov, Phys. Rev. Lett. **104**, 227003 (2010).

[52] M. V. Fistul', Sov. Phys. JETP **69**, 209 (1989).

[53] M. A. Itzler and M. Tinkham, Phys. Rev. B **53**, R11949 (1996).

[54] M. V. Fistul' and G. F. Giuliani, Phys. Rev. B **51**, 1090 (1995).

[55] R. Merservey and B. B. Schwartz, in *Superconductivity*, edited by R. D. Parks (Marcel Dekker, New York, 1969), Vol. 1, p. 126.

[56] J. Hauser, J. Low Temp. Phys. **7**, 335 (1972).

[57] A. I. Gubin, K. S. Il'in, S. A. Vitusevich, M. Siegel, and N. Klein, Phys. Rev. B **72**, 064503 (2005).

[58] J. Pearl, Appl. Phys. Lett. **5**, 65 (1964).

[59] V. N. Gladilin, J. Ge, J. Gutierrez, M. Timmermans, J. V. de Vondel, J. Tempere, J. T. Devreese, and V. V. Moshchalkov, New J. Phys. **17**, 063032 (2015).

[60] J. Gutierrez, B. Raes, J. Van de Vondel, A. V. Silhanek, R. B. G. Kramer, G. W. Ataklti, and V. V. Moshchalkov, Phys. Rev. B **88**, 184504 (2013).

[61] D. C. Tsui, Phys. Rev. Lett. **24**, 303 (1970).

[62] M. Noguchi, K. Hirakawa, and T. Ikoma, Phys. Rev. Lett. **66**, 2243 (1991).

[63] A. Barone and G. Paterno, *Physics and Applications of the Josephson Effect* (John Wiley & Sons, New York, 1982).